A Novel UAV Sensing Image Defogging Method

Tao Gao, Kun Li, Ting Chen, Mengni Liu, Shaohui Mei, Ke Xing, and Yong Hui Li

***Abstract*—Imaging of unmanned aerial vehicle easily suffer from haze, resulting in decline in the quality of required remote sensing images. The influence brings great challenges in later analysis and process. Although dark channel prior has acquired substantial achievements, some limitations, including imprecise estimation of atmospheric light, color distortion, and lower brightness of defogging image, still exist. In this article, to target these drawbacks, a novel defogging method for single image is proposed. First, a novel atmospheric scattering model is proposed to define the more accurate atmospheric light by introducing an adaptive variable strategy. Next, unlike traditional dark channel prior, a novel estimation method is presented by fusing dark and light channels to estimate more precise atmospheric light and transmittance. Then, we adopt the gray image corresponding to color image as a guidance image to refine the transmittance to further decrease the time complexity. Aiming at the region of low transmittance, a novel compensation function is created to improve the region of low transmittance and avoid color distortion. Moreover, a simple and effective calculation method is proposed to determine parameters in compensation function. Finally, the clear remote sensing image is established by an improved atmospheric scattering model. Extensive experiments on real-world datasets demonstrate that the proposed method outperforms several other state-of-the-art approaches both on subjective and objective quality evaluations.**

***Index Terms*—Dark channel prior (DCP), defogging, remote sensing image, unmanned aerial vehicle (UAV).**

I. Introduction

In RECENT years, owing to the advantages of agility, economy, convenience, and adaptability [1], unmanned aerial vehicle (UAV) remote sensing technology has been widely applied in disaster and environmental monitoring [2], agriculture [3], archaeology [4], disaster relief [5], target detection [6], and other fields. However, the imaging equipment of UAV is easily affected by haze, resulting in decline in the quality of required remote sensing images and leading to the difficulty in extracting effective information of images in later process, which seriously affects the analysis and judgment of visual system [7], [8]. Consequently, defogging of remote sensing image has important significance in UAV practical applications [9]–[11].

Manuscript received January 21, 2020; revised April 16, 2020 and May 17, 2020; accepted May 19, 2020. Date of publication May 29, 2020; date of current version June 11, 2020. This work was supported in part by the Fundamental Research Funds for the Central Universities, CHD, under Grant 300102249314, in part by the National Natural Science Foundation of China under Grant 61302150 and Grant 61703054, and in part by the Natural Science Foundation of Shanxi Province, China, under Grant 2019GY-039. *(Corresponding authors: Kun Li; Yong Hui Li.)*

Tao Gao, Kun Li, Ting Chen, Mengni Liu, Ke Xing, and Yong Hui Li are with the School of Information Engineering, Chang'an University, Xi'an 710064, China (e-mail: gtnwpu@126.com; 1026352280@qq.com; tchenchd@126.com; 814090112@qq.com; 928000394@qq.com; yhlichd@126.com).

Shaohui Mei is with the School of Electronics and Information, Northwestern Polytechnical University, Xi'an 710129, China (e-mail: meish@nwpu.edu.cn).

Digital Object Identifier 10.1109/JSTARS.2020.2998517

At present, the image defogging algorithms are roughly divided into two categories according to the physical model [12]–[14]: The first are the defogging algorithms based on image enhancement [15], and the other are defogging algorithms based on image restoration [16].

The defogging methods based on image enhancement utilize existing image processing technology without regard to the mechanism of image degradation and physical imaging model. Those methods mainly enhance the contrast of foggy images, highlight detail information, and improve visibility to achieve ideal defogging effect. The defogging methods based on image enhancement mainly include the Retinex theory [17], histogram equalization [18], and wavelet transform [19]. The Retinex model indicates that an image consists of two parts: incident component and reflected component, which represent brightness information and internal information, respectively [20]. Land [21] was the first to propose the Retinex theory based on color constancy, which is widely applied in image enhancement [22]. Based on the Retinex theory, the single-scale Retinex (SSR) algorithm [23] is mainly used for gray scale image enhancement. However, it cannot preserve both detail information and color restoration simultaneously. Based on SSR, a multiscale Retinex (MSR) algorithm [24] is proposed to enhance the colorful image. However, it will lead to color distortion to some extent. To overcome color distortion in MSR, an MSR with color restoration algorithm [25] is proposed. However, there is "Halo" effect in enhanced image, resulting in difficulty of the detail enhancement in bright region. Some relevant improved algorithms are presented on this basis [26]–[28], but none of them completely eliminate the "Halo" effect. The methods of histogram equalization stretch image contrast to achieve the enhancement of image contrast and obtain more details [29]–[31]. Nevertheless, those methods will lead to loss of details, color distortion, and overexposure when the concentration of fog is uneven or scene depth is discontinuous. Although Yelmanov and Romanyshyn [32]proposed an improved histogram equalization algorithm based on the evaluation of the two-dimensional probability distribution of image brightness, the problem of overexposure is not completely solved. Moreover, Ji *et al*. [33] proposed a histogram equalization method combined with median filtering, and Huang *et al*. [34] proposed a multiscale model combined with histogram characteristics. Although they are able to defog effectively for remote sensing image, the details of image will be blurred to different degrees. In addition, wavelet transform is another image enhancement method by improving its high-frequency component and reducing its low-frequency component [35]. However, wavelet transform has some limitations when fog concentration is large or uneven. Due to the fact that the information of scene depth is not considered, the

wavelet transform algorithms combined with YUV color space [36], physical model [37], and color-level compensation [38] are unable to achieve better visual effect in the fog scene. In brief, in the methods based on image enhancement, some drawbacks still exist, including color distortion, detail loss, and noise interference irrespective of image degradation mechanism and physical imaging model.

The defogging methods based on image restoration establish an image degradation model from the physical perspective. Those methods utilize prior theory to analyze the effect of environmental factors on image and establish corresponding mathematical model [39]. McCartney *et al*. [40] were the first to propose the atmospheric scattering model (ASM) and lay a solid foundation for image restoration methods. Some image restoration methods are proposed, mainly based on scene depth information [41], polarization property [42], prior information [43], etc. First, scene-depth-based methods estimate the transmission information by the scene depth and further restore the fog-free image by the ASM [44]–[47]. The acquisition of scene depth information is complex and difficult. Thus, the methods based on scene depth information have some weakness in practical application. Second, the methods based on polarization property mainly extract scattered atmospheric through the difference of polarized property between the nonpolarized scenery transmitted light and the partially polarized atmospheric scattered light [48]–[50]. However, it relies excessively on environment light, and the effectiveness of defogging is poor under dense fog conditions. Furthermore, it is a real challenge to acquire polarized image of some scenes [51]. Finally, the methods based on prior information conclude some regularities as the prior knowledge. Those methods mainly acquire the relevant parameters of the ASM and further generate fog-free image [52]–[53]. Based on the assumption that the surface shadow and transmission are locally unrelated, Fattle [54] proposed a method to estimate the transmission and atmospheric light. Nevertheless, it depends on the quality of input image to a great extent. Thus, the effect of defogging is poor when the signal-to-noise ratio of image is low. Tarel *et al*. [55] estimated atmospheric veil, assuming that atmospheric veil is less than the minimal component of the original foggy image. It can achieve the defogging effect but some color distortion still appear in the image. Tan *et al*. [56] observed that a clear image has high contrast and maximizing local contrast can be used for defogging. Nevertheless, it will produce "halo" effect. Among the defogging methods based on prior information, the method based on dark channel prior (DCP) is widely applied in defogging. He *et al*. [57] proposed a DCP theory that most areas in fog-free outdoor images contain some pixels that have very low intensity at least in one color channel. This prior theory is utilized to estimate the transmission map for defogging. In order to obtain higher quality image, many researchers present several methods based on this theory. Furthermore, some methods combined with DCP are proposed, including classification statistics [58], polarization information [59], machine learning [60], clustering [61], Gaussian filtering and bilateral filtering [62], energy function [63], and piecewise smoothing filtering [64]. To overcome the weaknesses, including atmospheric light overestimation, low transmission in sky area, and color distortion, Xu *et al*. [65] proposed a method based on DCP and light channel prior for defogging. Tufail *et al*. [66] proposed a method that is fusing the images obtained by RGB and YCbCr color space based on DCP. Wu [67] proposed a multiscale-guided filtering method, which applies DCP for defogging. Through the analysis of the DCP principle, Xie [68] proposed a novel DCP haze removal algorithm with the peak signal-to-noise ratio (PSNR). There are several defogging methods aiming at remote sensing images based on DCP [69]–[72]. Zhang *et al*. [71] proposed a defogging method based on dark channel and brightness enhancement, and its experimental results showed that the restored image had higher contrast and more detail information. In addition, Long *et al*. [72] proposed a method by utilizing a low-pass filter to refine atmospheric veil and redefine transmission, and it preserves more detail information and color information for restored image. The DCP is still one of the latest theories because of its strong applicability, detailed information, and colorful restored image in image defogging.

Although the existing algorithms achieve better performance, most of them are still unable to satisfy the quality requirements of defogging under different remote sensing scenes of UAV. There are still some shortcomings, such as unsuitability for the sky area, atmospheric light overestimation, transmission undervaluation, and color distortion. Aiming at solving the limitations of DCP, we propose a UAV sensing image defogging method named adaptive dual-channel prior fusion (ADPF): First, an improved ASM with different atmospheric intensities is proposed. Second, fusion of DCP and light channel prior is utilized to estimate atmospheric light and transmission map accurately. Then, the gray scale image is adopted as the guidance image to refine the transmission. Finally, the adaptive compensation function is utilized to improve the transmission in low-value area. Through a series of subjective and objective quality assessments, the experimental results show that our proposed ADPF obtains better performance compared with several state-of-the-art defogging algorithms. What is more, our improved algorithm relieves the DCP problems of contrast, brightness, and visual perception. The major contributions are as follows.

1) Focusing on the inaccurate definition of atmospheric light in the conventional ASM, the novel ASM is proposed to estimate the more accurate atmospheric light by introducing the adaptive variable strategy.
2) The traditional DCP theory always leads to imprecise estimation of atmospheric light and transmittance. To overcome this drawback, a novel estimation method is presented by fusing dark channel and light channel.
3) To further decrease the time complexity of defogging, we utilize the gray image corresponding to color image as guidance image to refine the transmittance. Moreover, the improvements not only preserve the edge information of scene depth, but also reduce time complexity.
4) Aiming at the shortcoming that DCP is unsuitable to sky area, a novel compensation function is created to improve the region of low transmittance and avoid color distortion. Furthermore, a simple and effective calculation method is proposed to determine parameters in compensation function. It greatly promotes the adaptability and effectiveness of the proposed algorithm.

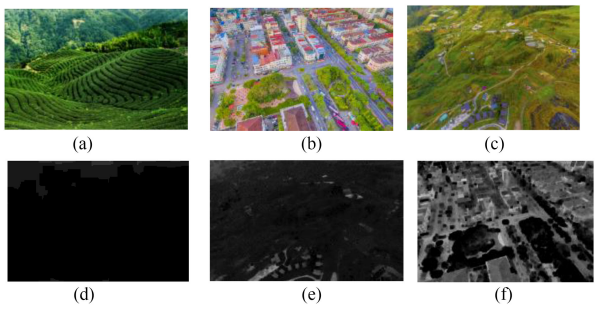

Fig. 1. (a)–(c) Fog-free images and (d)–(f) their corresponding dark channel images.

This article is organized as follows. Section I presents the background of image defogging and contributions of this article. Section II describes the defogging algorithm based on DCP. Section III gives the detailed description on our ADPF. Section IV verifies the effectiveness of ADPF by abundant experiments. Finally, Section V concludes this article.

II. Dark Channel Prior

A. Defogging Algorithm Based on the DCP

The ASM is utilized to describe the foggy image, given as [83]

$$I(\mathbf{x}) = J(\mathbf{x})t(\mathbf{x}) + A(1 - t(\mathbf{x})) \tag{1}$$

where $\mathbf{x}$ is the pixel coordinate. $I(\mathbf{x})$ represents the observed foggy image. $J(\mathbf{x})$ represents the fog-free image.A denotes the global atmospheric light, and $t(\mathbf{x})$ denotes the atmospheric transmission. The aim of defogging process is estimating $t(\mathbf{x})$ as well as A and then restoring $J(\mathbf{x})$.

According to (1), $J(\mathbf{x})t(\mathbf{x})$ represents direct attenuation, which indicates that part of the reflected light will be scattered, whereas the rest is obtained by acquisition device. $A(1 - t(\mathbf{x}))$ represents the atmospheric light scattered by atmospheric particles, which results in scene migration.

The transmission $t(\mathbf{x})$ under the condition of uniform distribution atmospheric is given as [83]

$$t(\mathbf{x}) = e^{-\beta d(\mathbf{x})} \tag{2}$$

where β represents the scattering coefficient of the atmosphere, and d represents the scene depth. For the fog-free image, $\beta \approx 0$ and $t(\mathbf{x}) \approx 1$. The effect of β is neglected and $I(x) \approx J(x)$. On the other hand, for the foggy image, $\beta > 0$, $t(\mathbf{x}) < 1$, and it becomes nonnegligible.

Based on the DCP proposed by He *et al*. [57], dark channel image of $J(\mathbf{x})$ is obtained by (3) [83]. Through various observations, they draw a conclusion that at least one color channel has very low intensity at some pixels in most of nonsky areas. Some examples of dark channel images are shown in Fig. 1

$$J^{\text{dark}}(\mathbf{x}) = \min_{c\in\{r,g,b\}} \left(\min_{\mathbf{y}\in\Omega(\mathbf{x})} (J^c(\mathbf{y})) \right) \tag{3}$$

where J^c donates a color channel. $\Omega(\mathbf{x})$ donates a local patch centered at $\mathbf{x}$, and $J^{\text{dark}}(x)$ represents a dark channel of image J, which is very low and tends to 0.

Dividing both sides of (1) by A^c

$$\frac{I^c(\mathbf{x})}{A^c} = \tilde{t}(\mathbf{x})\frac{J^c(\mathbf{x})}{A^c} + 1 - \tilde{t}(\mathbf{x}) \tag{4}$$

where $\tilde{t}(\mathbf{x})$ is set as a constant in local patch $\Omega(\mathbf{x})$. A^c represents the positive atmospheric light of a color channel, $c \in \{r, g, b\}$. $I^c(\mathbf{x})$ and $J^c(\mathbf{x})$ represent foggy image and fog-free image of a color channel, respectively.

After applying minimum filter for (4) on local patches and color channel, respectively, (5) [84]and (6) [84] are obtained

$$\min_{\mathbf{y}\in\Omega(\mathbf{x})} \left(\frac{I^c(\mathbf{y})}{A^c} \right) = \tilde{t}(\mathbf{x}) \min_{\mathbf{y}\in\Omega(\mathbf{x})} \left(\frac{J(\mathbf{y})}{A^c} \right) + 1 - \tilde{t}(\mathbf{x}) \tag{5}$$

$$\min_{c\in\{r,g,b\}} \left(\min_{\mathbf{y}\in\Omega(\mathbf{x})} \left(\frac{I^c(\mathbf{y})}{A^c} \right) \right) = \tilde{t}(\mathbf{x}) \min_{c\in\{r,g,b\}} \left(\min_{\mathbf{y}\in\Omega(\mathbf{x})} \left(\frac{J^c(\mathbf{y})}{A^c} \right) \right) + 1 - \tilde{t}(\mathbf{x}). \tag{6}$$

According to DCP, the coarse transmission $\tilde{t}(\mathbf{x})$ is determined as follows [84]:

$$\tilde{t}(\mathbf{x}) = 1 - \min_{c\in\{r,g,b\}} \left(\min_{\mathbf{y}\in\Omega(\mathbf{x})} \left(\frac{I^c(\mathbf{y})}{A^c} \right) \right). \tag{7}$$

Due to the requirement of aerial perspective, a constant parameter$\omega = 0.95$ is introduced into (7) to keep a small amount of fog for distant objects [57]. For the detailed value of constant parameter ω, readers are referred to literature [57]

$$\tilde{t}(\mathbf{x}) = 1 - \omega \min_{c\in\{r,g,b\}} \left(\min_{\mathbf{y}\in\Omega(\mathbf{x})} \left(\frac{I^c(\mathbf{y})}{A^c} \right) \right). \tag{8}$$

The top 0.1% brightest pixels in dark channel are picked. After determining the location of these pixels in the original image, the brightest pixel is set as atmospheric light A.

After estimating A and calculating $\tilde{t}(\mathbf{x})$, a fog-free image is reconstructed as follows [84]:

$$J(\mathbf{x}) = \frac{I(\mathbf{x}) - A}{\max\left(t(\mathbf{x}), t_0\right)} + A \tag{9}$$

where t_0 is a lower bound and generally set as 0.1 [57].

B. Guided Filtering Algorithm

Aiming at the block effect of dark channel image when defogging by coarse transmission, we need to further optimize the defogging process by refining transmission. The DCP utilizes soft matting to refine transmission, which consumes enormous memory by intensive computation. Therefore, the guided filtering algorithm is proposed to reduce the block effect and obtain precise fog-free image.

Guided filtering [73] is an edge smoothing filtering, which utilizes guidance image I to filter and preserve the overall characteristics of input image. Equation (10) indicates a linear relationship between output image q and guidance image$I$ in a window ω_k centered at the pixel k

$$q_i = a_k I_i + b_k \quad \forall i \in \omega_k \tag{10}$$

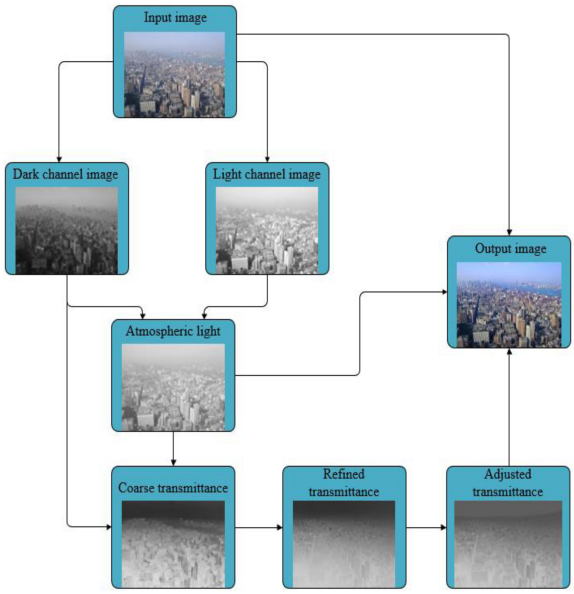

Fig. 2. Flowchart of algorithm proposed in this article.

where a_k and b_k are two linear constant coefficients, expressed as

$$a_k = \frac{\frac{1}{|w|}\sum_{i\in\omega_k} I_i p_i - \mu_k \bar{p}_k}{\sigma_k^2 + \in} \tag{11}$$

$$b_k = \bar{p}_k - a_k \mu_k. \tag{12}$$

Here, $|\omega|$ represents the pixel number of ω_k. u_k and σ_k^2 represent the mean and variance of I in ω_k, respectively. $\bar{p_k}$ represents the mean of p in ω_k.

In fact, pixels in I are affected by multiple filter windows, and output image q_i is required to be summed and averaged

$$q_i = \frac{1}{|w|}\sum_{k,i,i\in\omega_i}(a_k I_i + b_k) = \bar{a}_k I_i + \bar{b}_k \tag{13}$$

where $\bar{a}_k = \frac{1}{|\omega|}\sum_{k=\omega_j} a_k$ and $\bar{b}_k = \frac{1}{|\omega|}\sum_{k=\omega_j} \mathrm{b}_k$. $|\omega|$ represents the pixel number of ω_k. μ_k and σ_k^2 are the mean and variance of the guidance image I in ω_k, respectively.

III. Proposed Method

The flowchart of the proposed algorithm is shown in Fig. 2. First, based on the DCP and light channel prior, the dark channel image and the light channel image are obtained, respectively. Next, we utilize the two images to acquire the estimated atmospheric light. Subsequently, we estimate coarse transmission by dark channel image and atmospheric light, and then we refine transmission by guided filter and obtain the final transmission map by the adaptive compensation function. Finally, foggy remote sensing image, atmospheric light, and the final transmission map are substituted into our improved atmospheric light scattering model to obtain the fog-free image.

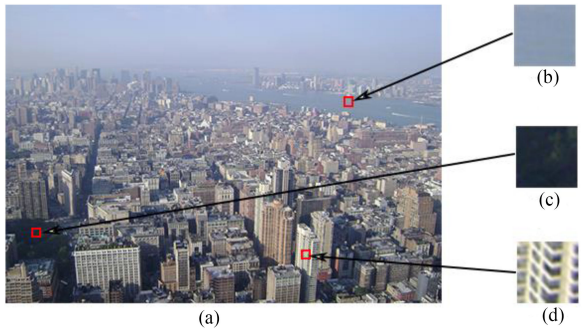

Fig. 3. Atmospheric light intensity in different regions.

A. Improved Atmospheric Light Scattering Model

Most of the algorithms are image restoration defogging methods based on ASM. In (1), the atmospheric light value A is a constant, i.e., the obtained atmospheric light value in an image is accurate and suitable for the whole image. However, based on abundant observations, the result reflected in Fig. 3 shows that the atmospheric light values of a bright and a dark pixel points are different.

Atmospheric light values of pixels are different in an image. For example, in Fig. 3(a)–(d), it can be clearly seen that atmospheric light values are different. Consequently, the ASM equation (1) is modified into the following:

$$I(\mathbf{x}) = J(\mathbf{x})t(\mathbf{x}) + A(\mathbf{x})(1 - t(\mathbf{x})). \tag{14}$$

As shown in (14), the atmospheric light value A in the original atmospheric light scattering model is improved to $A(\mathbf{x})$, that is, the uniform atmospheric light at each pixel in the original model is improved to the global variable with different atmospheric light values at each pixel, so as to make the estimation of atmospheric light more accurate and reasonable.

B. Estimation of Atmospheric Light Value and Transmission

Here, we apply the light channel prior theory for remote sensing image defogging. Similar to the DCP theory, it is obtained by observations, statistics, and experiments on a large number of outdoor foggy images. The basic light channel prior theory is that for most local areas of foggy images, there is at least one color channel with a large pixel value. For foggy image I, the expression of light channel I^{light} is defined as follows:

$$I^{\text{light}}(\mathbf{x}) = \max_{c\in\{r,g,b\}}\left(\max_{\mathbf{y}\in\Omega(\mathbf{x})}(I^c(\mathbf{y}))\right) \tag{15}$$

where I^c represents one color channel of the image I. $\Omega(\mathbf{x})$denotes a local region centered at pixel $\mathbf{x}$. The foggy remote sensing image and its light channel image are shown in Fig. 4.

The light channel prior theory reflects that the light channel value of a pixel point in foggy images is close to atmospheric light value of the fog-free image corresponding to foggy image [65], and the following formula is obtained:

$$I^{\text{light}}(\mathbf{x}) \to A^{\text{light}}(\mathbf{x}) \tag{16}$$

TABLE 1
PSNR AND SSIM OF THE RESTORED FOG-FREE IMAGE WITH DIFFERENT VALUES OF α AND β

	α=0.6 β=0.35	α=0.7 β=0.25	α=0.8 β=0.15	α=0.9 β=0.05	α=0.6 β=0.25	α=0.7 β=0.15	α=0.8 β=0.05	α=0.7 β=0.2
SSIM	17.1789	17.9890	16.7984	16.6131	23.7406	24.2623	23.8139	20.5028
PSNR	0.9220	0.9354	0.9284	0.9213	0.9471	0.9521	0.94180	0.9349

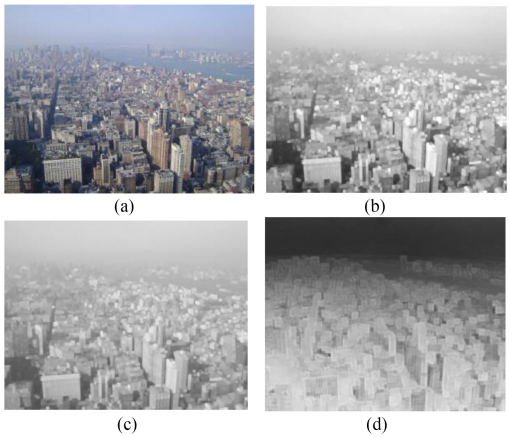

Fig. 4. (a) Original foggy remote sensing image. (b) Light channel image. (c) Atmospheric light image. (d) Estimated transmission map.

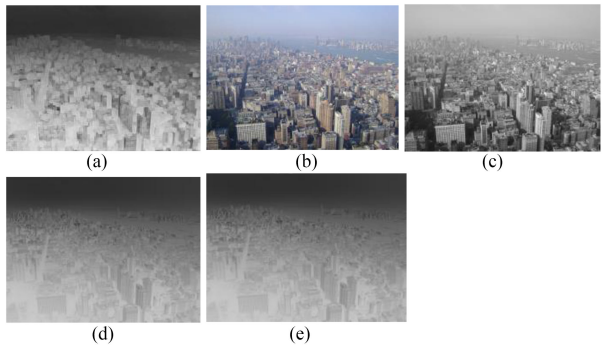

Fig. 5. Effect comparison of the two guidance images.

where $A^{\text{light}}(\mathbf{x})$ is the atmospheric light estimated by the light channel and is obtained by (15) and (16)

$$A^{\text{light}}(\mathbf{x}) = \max_{c\in\{r,g,b\}} \left(\max_{\mathbf{y}\in\Omega(\mathbf{x})} (I^c(\mathbf{y})) \right). \tag{17}$$

Furthermore, the atmospheric light can be obtained in (17) by the light channel image corresponding to the foggy image. In fact, we estimate the atmospheric light in 18) by combining the light channel prior with DCP

$$A(\mathbf{x}) = \alpha A^{\text{light}}(\mathbf{x}) + \beta A_0 \tag{18}$$

where A_0 refers to the atmospheric light value estimated by dark channel. α and β are adjusting parameters. A_0 can be acquired in Section II, always with overestimation as well as distortion of the restored fog-free images. Aiming at solving the above-mentioned problems, we select the pixels in the original image corresponding to the top 0.1% brightest pixels in the dark channel images and calculate the mean value of them as atmospheric light A_0. In fact, atmospheric light of the foggy image is higher than that of the fog-free image, i.e., $J(\mathbf{x}) \leq A(\mathbf{x})$. The ranges of transmission $t(\mathbf{x})$ are from 0 to 1, as shown in (2), and thus $J(\mathbf{x}) \leq I(\mathbf{x}) \leq A(\mathbf{x})$. Also, α and β satisfy $\alpha + \beta < 1$.

Since the pixel values of light channel are close to atmospheric light of fog-free image, we should set the weight of atmospheric light based on light channel with a larger value and weight of atmospheric light based on dark channel with a lower value. Based on relevant experiments, PSNR [81] and structural similarity index measurement (SSIM) [80] of the restored fog-free image with different α and β are listed in Table I.

In Table I, PSNR and SSIM of the restored image are maximum if α= 0.7 and β= 0.15, which indicate that the restored image is of the highest quality. Therefore, we set α= 0.7 and β= 0.15. The final atmospheric light image can be found in Fig. 4.

Based on our improved ASM and atmospheric light obtained by light channel prior and DCP, the estimated transmission $t'(\mathbf{x})$ in (8) is modified as follows:

$$t'(\mathbf{x}) = 1 - \omega \frac{\min\limits_{c\in\{r,g,b\}} \left(\min\limits_{\mathbf{y}\in\Omega(\mathbf{x})} (I^c(\mathbf{y})) \right)}{A(\mathbf{x})}. \tag{19}$$

Then, the estimated transmission map is calculated by (19) and is shown in Fig. 4.

C. Refined Transmission Map

In the process of acquiring transmission $t'(\mathbf{x})$, we adopt the DCP and light channel prior, which contain the step of regional filtering. The regional filtering will lead to block effect and lose much detail information. To overcome the drawbacks, guided filtering is utilized to refine transmission and set transmission $t'(\mathbf{x})$ as the input image of the guided filtering. Meanwhile, the guidance image needs to have the same edge information as the input image. Therefore, the gray scale image of original image and the original image both can be used as the guidance image, respectively, as shown in Fig. 5.

The transmission map obtained by (19) is shown in Fig. 5(a). The original image [shown in Fig. 5(b)] and the gray scale image [shown in Fig. 5(c)] are, respectively, utilized as guidance images to obtain refined transmission maps, as shown in Fig. 5(d) and (e). Visually, the two refined transmission maps differ slightly since both original image and gray scale image have the same gradient and detail information. The computation time and information entropy of two defogged images are respectively obtained from the guidance images, as listed in Table II. The size

TABLE II
FILTERING RESULTS OF TWO KINDS OF GUIDE GRAPHS

Guidance image	time/s	Entropy (bit/pixel)
RGB image	4.5930	7.5910
Gray scale image	0.3002	7.5903

of guidance image is 768×1024 pixels, and the size of filtering window is selected as 60×60 pixels.

As listed in Table II, the processing speed of gray scale image is obviously faster than the RGB image. Especially, there is almost no difference between their entropies. Therefore, in this article, the gray scale image is selected as guidance image to preserve detailed edge information.

D. Adaptive Transmission Compensation Function

Based on abundant observations, the DCP may be invalid in sky area. Due to the fact that nearly all dark channel values are large in sky area, the estimated transmission calculated by (19) is lower than the real transmission. Aiming at overcoming the drawback, we construct an adaptive compensation function to improve the transmission of invalid area and avoid color distortion.

The transmission calculated by the compensation function is expressed as follows:

$$t(\mathbf{x}) = t''(\mathbf{x}) + \Delta t(\mathbf{x}) \tag{20}$$

where $t''(\mathbf{x})$ denotes refined transmission by guided filtering. $\Delta t(\mathbf{x})$ is compensation function. An inverse relation between transmission and scene depth is reflected in (2). According to the definition of transmission, we conclude that $0 < \Delta t(\mathbf{x}) < 1$, and the compensation function is constructed as follows:

$$\Delta t(\mathbf{x}) = \exp(-kt''(\mathbf{x})) \tag{21}$$

where k is used to adjust the compensation intensity for transmission. The sky area with low transmission $t''(\mathbf{x})$has high compensation value, whereas nonsky area has low compensation value. Equation (22) is obtained by (20) and (21)

$$t(\mathbf{x}) = t''(\mathbf{x}) + \exp(-kt''(\mathbf{x})) \tag{22}$$

where $t(\mathbf{x})$ denotes a concave function related to $t''(\mathbf{x})$. The minimum value point $(t_p, t_{\min})$ of the function is calculated as follows:

$$\begin{cases} t_p = \text{In } k/k \\ t_{\min} = t_p + \exp(-kt_p) = \text{In } k/k + 1/k \end{cases}. \tag{23}$$

Since there is low transmission and no obvious change of the scene depth in sky area, we set a lower bound of $t(\mathbf{x})$, as shown in the following equation:

$$t(\mathbf{x}) \begin{cases} t''(\mathbf{x}) + \exp(-\text{kt}''(\mathbf{x})) & t''(\mathbf{x}) \geq t_p \\ t_{\min} & t''(\mathbf{x}) < t_p \end{cases}. \tag{24}$$

In order to increase the adaptability of compensation function, we adaptively adjust the parameter k according to the foggy image. The adjustment intensity for transmission under different k values is shown in Fig. 6.

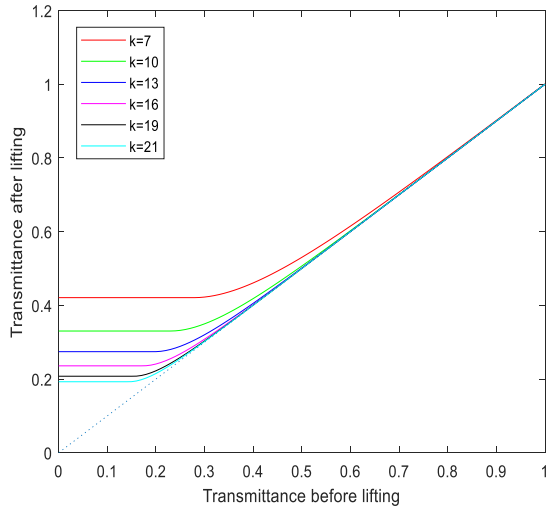

Fig. 6. Elevation of $t''(\mathbf{x})$ and $t(\mathbf{x})$ curve under different k.

TABLE III
PERCENTAGE OF THE NUMBER OF k VALUES IN THE NUMBER OF SUCH IMAGES WHEN THE REMOTE SENSING IMAGES CONTAINING THE SKY REGION OBTAIN THE BEST INDEXES

	k =6	k =7	k =8	k =9	k =10
percentage	7.7%	38.5%	30.7%	15.4%	7.7%

TABLE IV
PERCENTAGE OF THE NUMBER OF k VALUES IN THE NUMBER OF SUCH IMAGES WHEN THE REMOTE SENSING IMAGES THAT DO NOT CONTAIN OR CONTAIN A SMALL AMOUNT OF THE SKY REGION OBTAIN THE BEST INDEXES

	k =18	k =19	k =20	k =21	k =22
percentage	5.4%	16.2%	59.5%	16.2%	2.7%

The result shown in Fig. 6 reflects that the compensation function effectively improves transmission in low-value area, whereas there is nearly no change in high-value area, which completely meets our original motivation.

In order to determine the optimal k value in the two types of remote sensing images that contain the sky region and those that do not or contain a small amount of the sky region, we select 50 remote sensing images, as shown in Fig. 10. We divide them into the above-mentioned two categories to obtain the fogless image recovered from each image under different k values, and then the PSNR [81] and SSIM [80] indexes of different fogless images are obtained after calculating. Finally, we obtain the percentage of the number of different k values in the number of this type of images, as shown in Tables III and IV.

According to the analysis presented in Tables III and IV, for the remote sensing images containing the sky region, the transmittance of the sky region needs to be greatly improved. Generally, the k value is set to 7–9. For remote sensing images that do not contain or contain a small amount of the sky region, there is no need to do much lifting, and the k value is set to about

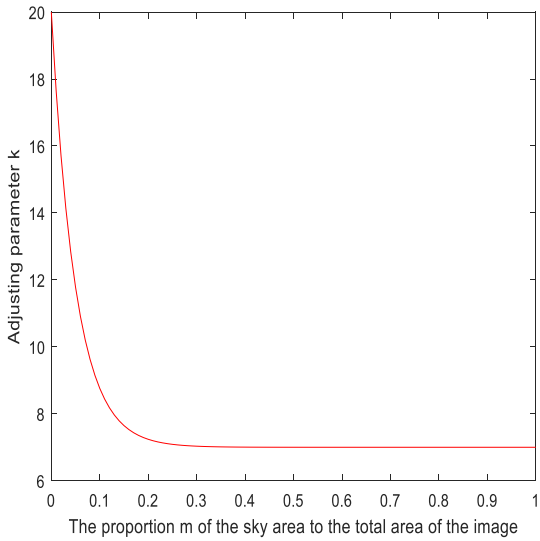

Fig. 7. Image of the relationship between k and m.

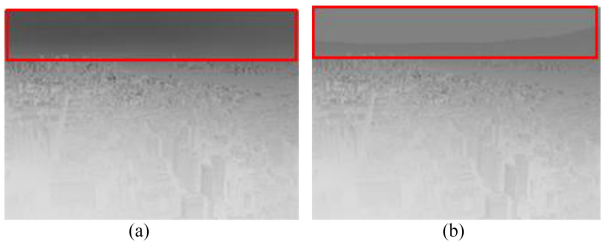

Fig. 8. (a) Refined transmission map. (b) Transmission map adjusted by the adaptive compensation function.

20. To sum up, k is set as a function related to the area of the sky reginal

$$k = 7 + 13\exp(-20\ m). \tag{25}$$

In general, the transmission of the sky region is less than 0.14. m is the proportion of the sky region in whole image. The relation function between k and m is shown in Fig. 7.

The transmission map adjusted by the adaptive compensation function and the original refined transmission map are shown in Fig. 8.

As shown in Fig. 8(a), the transmission is low in the red rectangle, and it will lead to color distortion in later defogging process. In Fig. 8(b), the transmission is obviously improved by the adaptive compensation function, as shown in the red rectangle. Moreover, there is no obvious change outside the red rectangle.

E. Reconstruction of Fog-Free Image

Based on the improved atmospheric light scattering model, we utilize estimated atmospheric light and transmission to restore fog-free image. Equation (14) is transformed into the following equation:

$$J(\mathbf{x}) = A(\mathbf{x}) + \frac{I(\mathbf{x}) - A(\mathbf{x})}{t(\mathbf{x})}. \tag{26}$$

For example, a restored image is calculated by (26) and shown in Fig. 9.

Fig. 9. Original remote sensing image and restored image.

IV. Experiment

A. Pseudocode of Algorithm Process and Experimental Settings

The pseudocode of algorithm process is shown as follows.

The defogging algorithm in this work
Input: foggy image $I(\mathbf{x})$;
1. Calculating the dark channel $I^{\mathrm{dark}}(\mathbf{x})$ of remote sensing foggy images by Eq. (3).
2. Calculating the light channel $I^{\mathrm{light}}(\mathbf{x})$ of remote sensing foggy images by Eq. (15).
3. Calculating atmospheric light $A^{\mathrm{light}}(\mathbf{x})$ estimated by light channel in Eq. (16).
4. Picking the top 0.1% brightest pixels in $I^{\mathrm{dark}}(\mathbf{x})$. After determining the location in original image of these pixels, the mean value of these pixel points is set as atmospheric lightA_0.
5. Calculating final atmospheric light $A(\mathbf{x})$ by Eq. (18).
6. Calculating coarse transmission map $t'(\mathbf{x})$ by Eq. (19).
7. Utilizing the gray scale image as guidance image to obtain refined transmission map $t''(\mathbf{x})$.
8. The proportion parameter m is obtained from the refined transmission map$t''(\mathbf{x})$.
9. Calculating adjusting parameter k by Eq. (25).
10. Calculating final adaptive adjustment transmission map $t(\mathbf{x})$ by Eq. (24).
11. Obtaining clear remote sensing image $J(\mathbf{x})$ by Eq. (26).

Output: clear image $J(\mathbf{x})$.
End

The specific experimental environment settings are shown in Table V.

B. Image Quality Evaluation

In order to evaluate defogging performance, we conduct several experiments compared with some state-of-the-art defogging algorithms, including Retinex [24] and the ones presented by Fattle [54], Tarel [55], He [57], Xu [65],Tufail [66], Wu [67], and Xie [68], by objective and subjective evaluations.

1) Subjective Quality Evaluation: Because human is the ultimate percipient of image, subjective quality evaluation is determined by the personal visual perception. In this section, we adopt Ma's method [74] to evaluate subjective quality of

TABLE V
EXPERIMENTAL ENVIRONMENT SETTINGS

index	environment	configuration
1	operating system	Window 10 with 64 bit
2	CPU	3.2GHz
3	memory	8G
4	hard disk	1T
5	programming tool	Matlab R2018a

defogged images. Here, we select 50 foggy remote sensing images containing different scenes, fog density, and photographic distance, as shown in Fig. 10.

We establish 50 datasets for subjective quality evaluation, including 50 original foggy remote sensing images and 400 restored images from 8 kinds of defogging algorithms. For example, one of 50 datasets is shown in Fig. 11.

We conduct our experiment at the laboratory of the Department Of Electronics, Chang'an University, where light condition is well, what is more, its ceiling, floor, and walls are nonreflective. Experimental images are displayed with a resolution of 2560×1600, and the display is calibrated according to ITU-R BT.500 [75]. We totally select 40 volunteers, including 15 women and 25 men, between the ages of 22 and 28 to participate in subjective evaluation experiment and limit the experimental time to 40 min on each volunteer to avoid visual fatigue; moreover, volunteers are allowed to adjust their position and angle for better observation. Specifically, there are eight images in each dataset, and each dataset is showed randomly to volunteers, and volunteers are asked to make integral score on each image with the range of 1–10. The score represents the image quality. None of the volunteers have any experience with image processing. Moreover, any background information of image is not provided to volunteer, and the score of each image is only determined by personal preferences and subjective feelings. At the end of the experiment, we calculate the mean opinion score (MOS) given by volunteers for final subjective evaluation quality score. The compared results reported in Fig. 12 indicate that the proposed algorithm in this article acquires the highest MOS compared with other state-of-the-art algorithms and shows rich color, attractive subjective visual perception, and better defogged effect.

2) Objective Quality Evaluation: Image objective quality evaluation criterion is roughly divided into three categories: full-reference image quality assessment [76], reduced-reference image quality assessment [77], and no-reference image quality assessment [78]. Full-reference image quality assessment and reduced-reference image quality assessment need to have clear original image corresponding to foggy image. Therefore, their application scope is small, and it is difficult to meet the conditions in the practical application. Consequently, we adopt no-reference image quality assessment, including four evaluation indexes universal quality index (UQI) [79], SSIM [80], PSNR [81], and information entropy H [82], to evaluate the performance of the proposed method compared with six kinds of mainstream defogging algorithms.

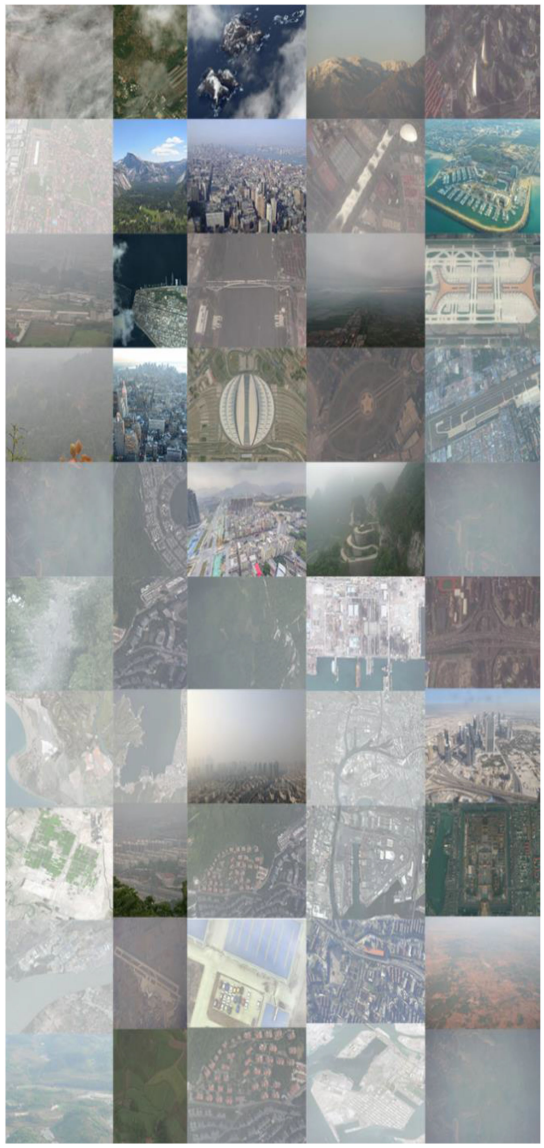

Fig. 10. Fifty foggy images.

The definition for UQI is

$$\mathrm{UQI} = \frac{\sigma_{xy}}{\sigma_x \sigma_y} \cdot \frac{2\bar{x}\bar{y}}{(\bar{x})^2 + (\bar{y})^2} \cdot \frac{2\sigma_x \sigma_y}{\sigma_x^2 + \sigma_y^2} \tag{27}$$

where $x = \{x_i | i = 1, 2, \ldots, N\}$ is the original image. $y = \{y_i | i = 1, 2, \ldots, N\}$ is the testing image, specifically, $\bar{x} =$

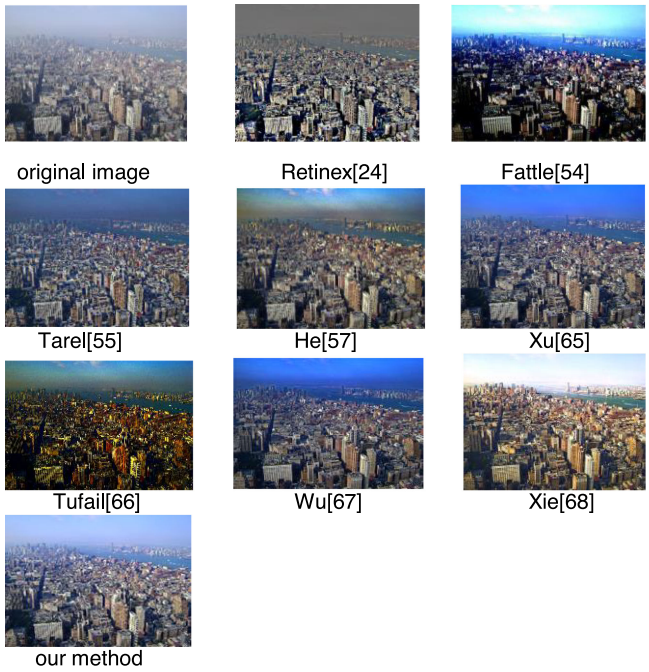

Fig. 11. Images contained in a dataset

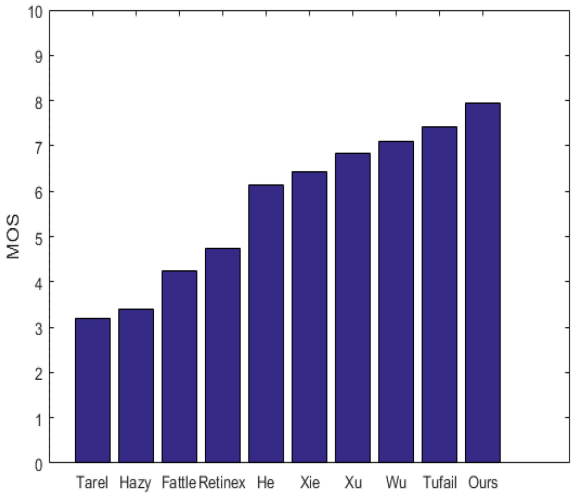

Fig. 12. MOS of original image and clear images.

$\frac{1}{N}\sum_{i=1}^{N} x_i, \bar{y} = \frac{1}{N}\sum_{i=1}^{N} y_i, \sigma_x^2 = \frac{1}{N-1}\sum_{i=1}^{N}(x_i - \bar{x})^2, \sigma_y^2 = \frac{1}{N-1}\sum_{i=1}^{N}(y_i - \bar{y})^2$, and $\sigma_{xy} = \frac{1}{N-1}\sum_{i=1}^{N}(x_i - \bar{x})(y_i - \bar{y})$.

The range of UQI is $[-1,1]$. The closer the value is to 1, the better the quality of the contrast image is. When the original image and the contrast image are the same, the value is 1.

The formula for SSIM is given as follows:

$$\mathrm{SSIM}(A,B) = \frac{2\overline{AB} + C_1}{\bar{A}^2 + \bar{B}^2 + C_1} \times \frac{2\sigma_{AB} + C_2}{\sigma_A^2 + \sigma_B^2 + C_2} \tag{28}$$

where A is the original foggy image, and B is the testing image that refers to the restored image. $\overline{A}$ and $\overline{B}$ are the average gray values of images A and B, respectively.σ_A and σ_B are the variances of $A$and B, respectively. σ_{AB} is the covariance. C_1,C_2, and C_3 are introduced constants. Besides, in practical application, $\alpha = \beta = \gamma = 1$ and $C_3 = \frac{C_2}{2}$. SSIM is acquired in brightness, contrast, and structural similarity with the range of [0,1]. The closer it is to 1, the higher the structural similarity of the two images is, the less the distortion is, and the better the image quality is.

The formula for PSNR is given as follows:

$$\mathrm{PSNR} = -10\log\frac{\mathrm{MSE}}{A^2} = 10\log\frac{\sum_1^M\sum_1^N\left[\hat{f}(x,y) - f(x,y)\right]^2}{M * N * A^2} \tag{29}$$

where A is the maximum possible pixel value for an image. $f(x,y)$is the original image, $\hat{f}(x,y)$ is the restored image, and M and N, respectively, represent the length and width of the image. MSE is defined as the mean square error of the image. The unit of PSNR is decibel (db). The higher the value is, the less the distortion is.

The formula for information entropy *H* is given as follows:

$$H = -\sum_{0}^{255} p_i Inp_i \tag{30}$$

where p_i is the ratio of the number of pixels in the image with a gray value$i$ to the total number of pixels in the image.

We conduct objective quality evaluation on remote sensing images in five different scenes. Moreover, we carry out the subjective comparison analysis before the objective data comparison.

2) a) First set of comparative experiments: We conduct relevant experiments in city scene compared with other eight state-of-the-art defogging algorithms. A total of nine pictures without fog are used for experimental comparison. The experimental results are shown in Fig. 13.

In Fig. 13, the restored image defogged by Retinex [24] appears overall gray. The result of defogging by Fattal's method [54] method appears dark in buildings and slightly blue in partial sky area. The restored image by Tarel's [55] method is generally blurred and appears gray. The image by He's [57] method and Wu's [67] method shows color distortion in sky area. In the restored images by Xu's [65] method a small amount of fog in distant buildings still exist. Tufail's [66] method performs low degree of defogging. The sky area of the restored image based on Xie's [68] method is yellowish, resulting in color distortion. In contrast, image defogged by ADPF has the least distortion and more natural visual effect.

The objective evaluation results of urban remote sensing images are listed in Table VI, including UQI, SSIM, PSNR, and *H*. In order to intuitively compare the performances, the results presented in Table VI are shown as bar charts in Figs. 14 and 15. In conclusion, all the four indicators of ADPF are the highest, which indicates that ADPF achieves the best defogging effect in this group.

b) Second set of comparative experiments: The image utilizes foggy remote sensing images in villages and towns as the reference image. The defogging comparison between eight state-of-the-art methods and ADPF is shown in Fig. 16. A total of nine pictures without fog are used for experimental comparison.

In Fig. 16, the upper area of the restored image by Retinex [24] appears gray and heavy fog. The result of Fattal's [54]

TABLE VI
OBJECTIVE EVALUATION RESULTS OF REMOTE SENSING FOGGY IMAGE IN URBAN AFTER DEFOGGING

	Retinex algorithm	Fattal's algorithm	Tarel's algorithm	He's algorithm	Xu's algorithm	Tufail's algorithm	Wu's algorithm	Xie's algorithm	ADPF algorithm
UQI	0.6169	0.5327	0.7450	0.8250	0.8991	0.6988	0.8036	0.9039	0.9260
SSIM	0.7077	0.5938	0.8219	0.9098	0.9301	0.6873	0.8248	0.9135	0.9529
PSNR	11.3233	7.4651	16.1212	16.0164	17.6974	12.4275	14.1088	17.6827	20.0047
H	7.5033	6.7462	7.2082	6.9900	6.8588	6.9372	6.9523	6.8220	7.9853

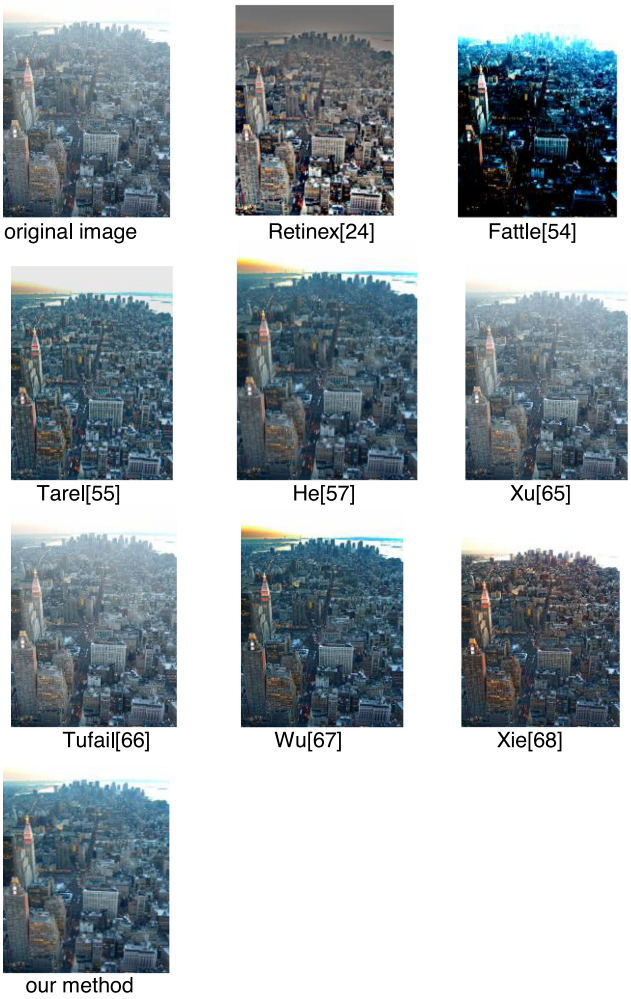

Fig. 13. Remote sensing image of urban under foggy condition.

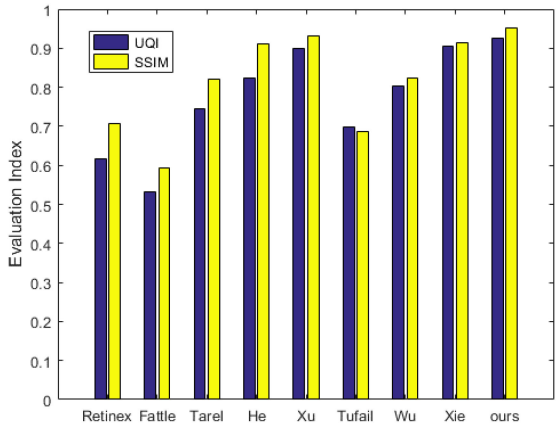

Fig. 14. Results bar chart of UQI and SSIM.

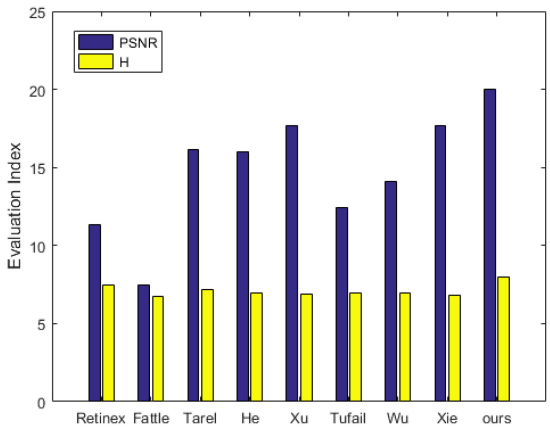

Fig. 15. Results bar chart of PSNR and *H*.

method shows obviously white on the top area of the restored image. The defogging effect of Tarel's method [55] is poor. The defogging image by He's [57] method shows good performance but appears overall dark and low contrast. The result of Xu's [65] method shows obvious distortion on top of the restored image. The lower half part of defogged image appears yellow and shows color distortion based on Tufail's [66] method. The top area of the recovered image based on Wu's [67] method is severely distorted, presenting a large area of white. Xie's [68] method also produces significant distortion in the upper half of the image. On the contrary, the result of ADPF shows natural visual effect with bright color and has the best sense of scene depth.

Table VII shows the objective evaluation results of urban foggy remote sensing image by using UQI, SSIM, PSNR, and information entropy *H*. Fig. 17 shows bar charts of UQI and SSIM corresponding to Table VII, and Fig. 18 shows bar charts of PSNR and information entropy *H* corresponding to Table VII. It can be seen from the above that although the information entropy index of ADPF is about 3.4% lower than that of Xu's algorithm, the other three indexes of ADPF outperform Xu's algorithm by a large margin and acquire the highest results among

TABLE VII
OBJECTIVE EVALUATION RESULTS OF REMOTE SENSING FOGGY IMAGE IN VILLAGE AFTER DEFOGGING

	Retinex algorithm	Fattal's algorithm	Tarel's algorithm	He's algorithm	Xu's algorithm	Tufail's algorithm	Wu's algorithm	Xie's algorithm	ADPF algorithm
UQI	0.6006	0.2536	0.5848	0.4557	0.5668	0.5372	0.7639	0.8936	0.9345
SSIM	0.7592	0.3925	0.7745	0.5945	0.7393	0.6279	0.8042	0.8260	0.9734
PSNR	15.2638	10.7623	18.6816	10.7444	14.7037	15.0034	15.3117	15.1631	24.3335
H	6.3981	6.9257	6.5384	6.9355	7.3609	6.7018	6.9823	6.8896	7.1071

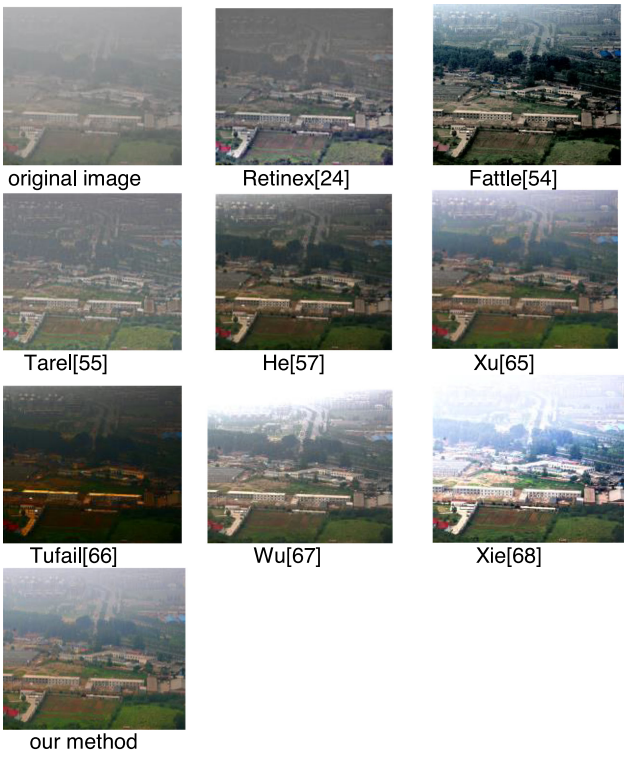

Fig. 16. Remote sensing foggy image in villages and towns after defogging.

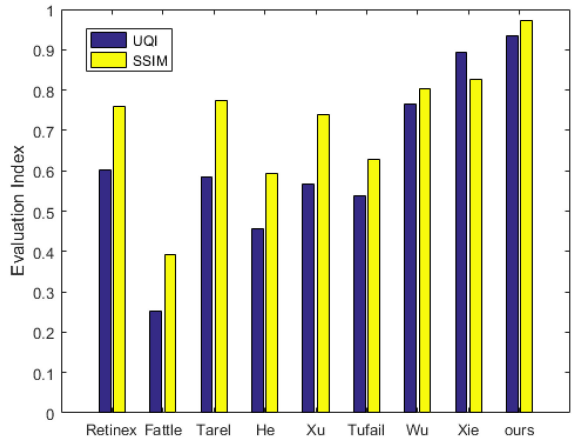

Fig. 17. Results bar chart of UQI and SSIM.

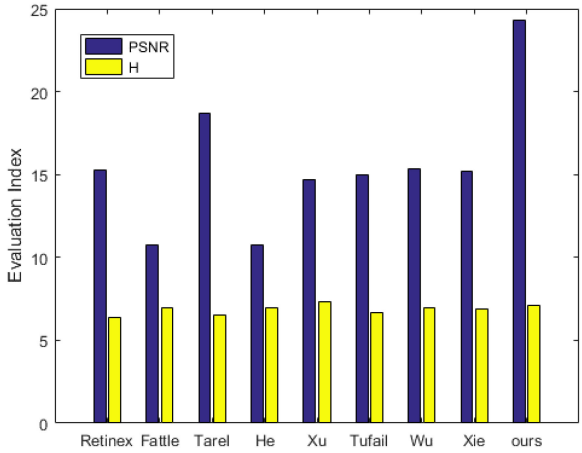

Fig. 18. Results bar chart of PSNR and *H*.

all comparable algorithms. In summary, ADPF can achieve the best defogging effect in this group of experiments.

c) Third set of comparative experiments: We conduct relevant experiments in farmland scene compared with other eight state-of-the-art defogging algorithms. A total of nine pictures without fog are used for experimental comparison. The experimental results are shown in Fig. 19.

In Fig. 19, the roads of the restored image appear purple and distorted by Retinex [24]. The result of defogging by Fattal's [54] shows lots of black spots. The restored image by Tarel's method [55] has less distortion but some fog still exists. Although the restored images defogged by He's [57] and Tufail's [66] method are bright and colorful and have better visual effect, the road appears green. Xu's [65] method performs well with less distortion, but the degree of defogging is poor. Compared with the original foggy image, the fog-free image restored by Wu's [67] method does not change significantly. The distortion is evident in the upper right corner of the restored image based on Xie's [68] method, where the field changes from green to purple. By contrast, the proposed algorithm significantly enhances the image contrast with the least distortion and achieves the best visual effect.

Table VIII shows the objective evaluation results of clear farmland remote sensing images by using UQI, SSIM, PSNR, and *H*. In order to intuitively compare the performances, Fig. 20 represents bar charts of UQI and SSIM corresponding to Table VIII, and Fig. 21 shows bar charts of PSNR and *H* corresponding to Table VIII. As discussed above, ADPF achieves the best performance for the four indicators.

d). Fourth set of comparison experiment: We conduct relevant experiments in suburb scene compared with other eight state-of-the-art defogging algorithms. A total of nine pictures

TABLE VIII
OBJECTIVE EVALUATION RESULTS OF FOGGY REMOTE SENSING IMAGES IN FARMLAND AFTER FOG REMOVAL

	Retinex algorithm	Fattal's algorithm	Tarel's algorithm	He's algorithm	Xu's algorithm	Tufail's algorithm	Wu's algorithm	Xie's algorithm	ADPF algorithm
UQI	0.2638	0.1222	0.5006	0.5821	0.7355	0.5380	0.7756	0.7783	0.8101
SSIM	0.4213	0.3671	0.7479	0.7679	0.8913	0.6342	0.7656	0.8509	0.9337
PSNR	17.9657	12.9156	20.5897	18.6206	23.2229	19.0584	19.4365	24.3544	26.6593
H	7.0438	7.1483	6.5126	6.2362	6.4910	6.7432	6.2757	6.2113	7.5209

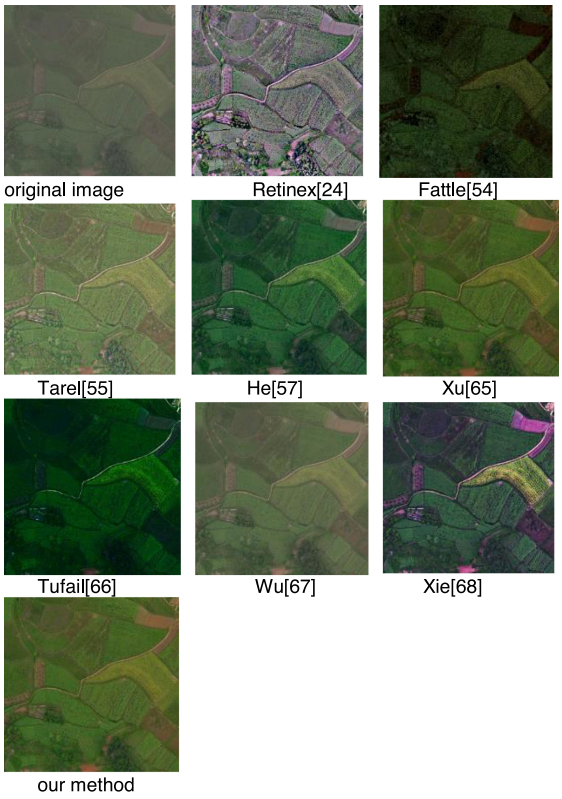

Fig. 19. Remote sensing image of farmland under foggy day.

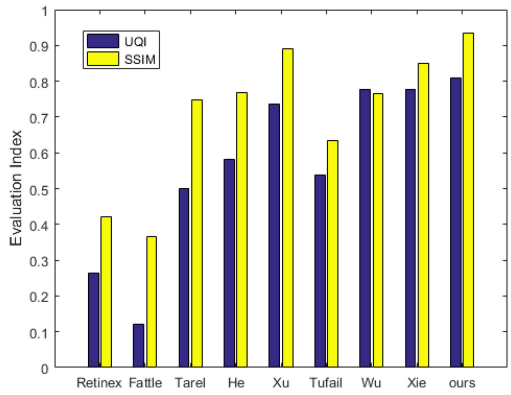

Fig. 20. Results bar chart of UQI and SSIM.

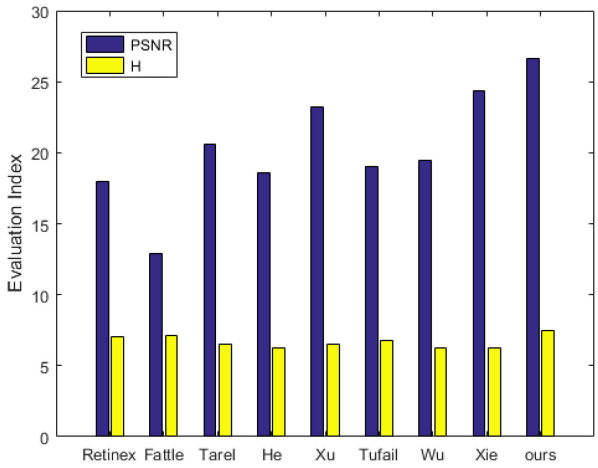

Fig. 21. Results bar chart of PSNR and *H*.

without fog are used for experimental comparison. The experimental results are shown in Fig. 22.

In Fig. 22, it can be observed that the image defogged by the Retinex [24] appears gray, and forest area appears severely distorted. The restored image by Fattal's [54] method appears white and has poor effect. The image defogged by Tarel's [55] method differs slightly from the original image. In addition, the defogged image by He's [57] method appears slightly gray. The image defogged by Tufail's [66] method appears dark and has loss of detail information. Based on Wu's [67] method, the picture appears black on the whole after removing the fog and losing a lot of details. The whole restored image based on Xie's [68] method appears in light green. It clearly shows that Xu's [65] method and ADPF have better visual effect. Furthermore, the image defogged by ADPF is more natural.

Table IX shows the objective evaluation results of clear suburb remote sensing images by using UQI, SSIM, PSNR, and *H*. In order to intuitively compare the performances, the results presented in Table IX are shown as bar charts in Figs. 23 and 24. Although the PSNR of ADPF is lower than that of Tarel's algorithm, all the other three indexes of ADPF achieve the best results among all comparable algorithms. All in all, ADPF achieves the best defogging effect in this group of experiments.

e) Fifth set of comparative experiments: We conduct relevant experiments in airport scene compared with other eight state-of-the-art defogging algorithms. A total of nine pictures without fog are used for experimental comparison. The experimental results are shown in Fig. 25.

In Fig. 25, the restored image by Retinex appears slightly white [24]. The result of defogging by Fattal's [54] method

TABLE IX
OBJECTIVE EVALUATION RESULTS OF FOGGY REMOTE SENSING IMAGES IN SUBURB AFTER FOG REMOVAL

	Retinex algorithm	Fattal's algorithm	Tarel's algorithm	He's algorithm	Xu's algorithm	Tufail's algorithm	Wu's algorithm	Xie's algorithm	ADPF algorithm
UQI	0.2056	0.2034	0.6441	0.5078	0.5766	0.3225	0.4631	0.6502	0.6900
SSIM	0.2542	0.2117	0.7438	0.5696	0.6814	0.3620	0.4567	0.7780	0.7907
PSNR	12.0407	12.1110	18.1393	13.5668	11.9158	12.9010	11.1985	12.1958	14.0930
H	7.6607	6.6934	6.9041	6.4084	6.6994	6.3710	6.8265	6.7369	7.7173

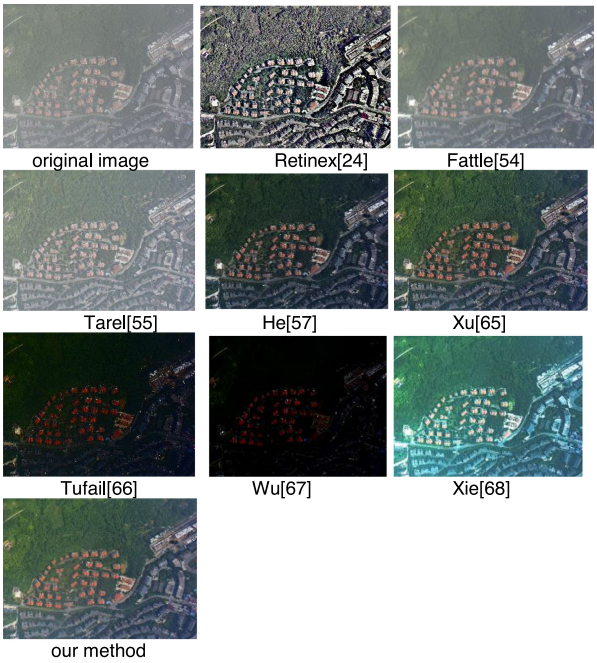

Fig. 22. Remote sensing image of suburb under foggy days.

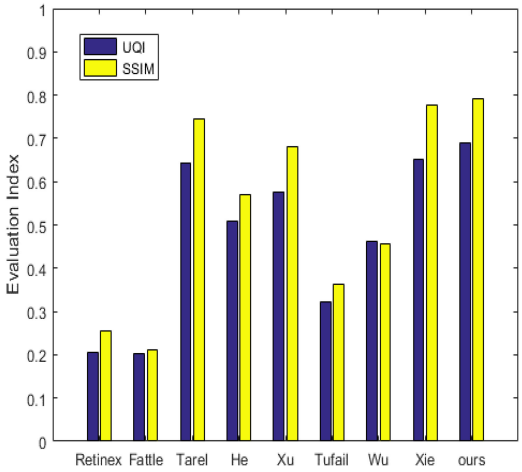

Fig. 23. Results bar chart of UQI and SSIM.

shows large dark area on the edge of the restored image. Image defogged by Tarel's [55] method performs low degree of dehazing. The image appears dark and distorted based on He's method [57]. The defogging effect of Xu's [65] appears overall yellow as well as slightly blue in some areas. The image restored

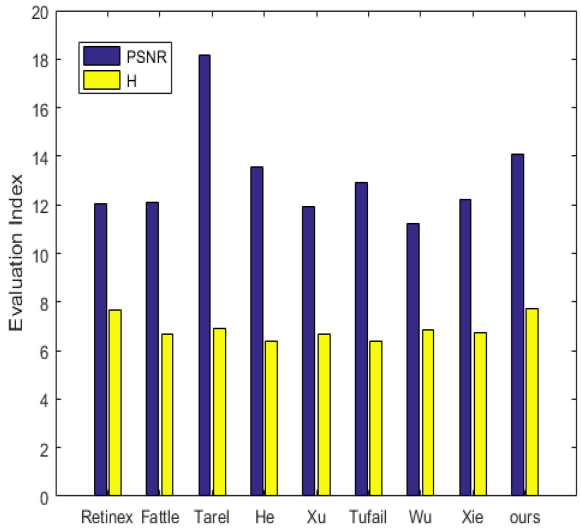

Fig. 24. Results bar chart of PSNR and *H*.

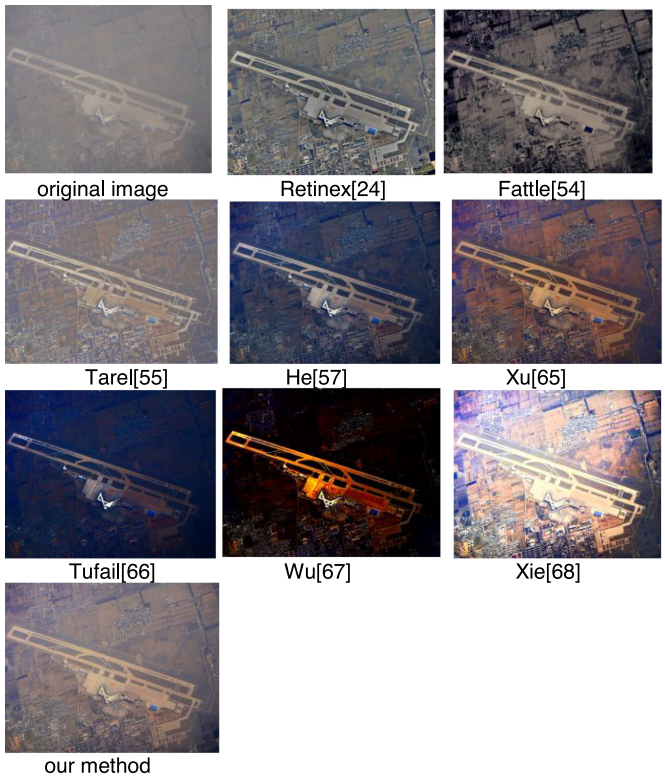

Fig. 25. Dehazing contrast maps of foggy remote sensing images of airport.

TABLE X
OBJECTIVE EVALUATION RESULTS OF FOGGY REMOTE SENSING IMAGES IN AIRPORT AFTER FOG REMOVAL

	Retinex algorithm	Fattal's algorithm	Tarel's algorithm	He's algorithm	Xu's algorithm	Tufail's algorithm	Wu's algorithm	Xie's algorithm	ADPF algorithm
UQI	0.4060	0.3087	0.5439	0.4706	0.4947	0.2576	0.8718	0.8263	0.9150
SSIM	0.6208	0.5324	0.7893	0.6120	0.6834	0.3508	0.7421	0.7184	0.9700
PSNR	17.8325	12.7368	25.4735	11.0094	13.6986	8.2599	17.9340	17.4862	26.1381
H	6.8075	6.6813	6.6986	6.4850	6.6760	5.9768	6.5350	7.0960	7.4339

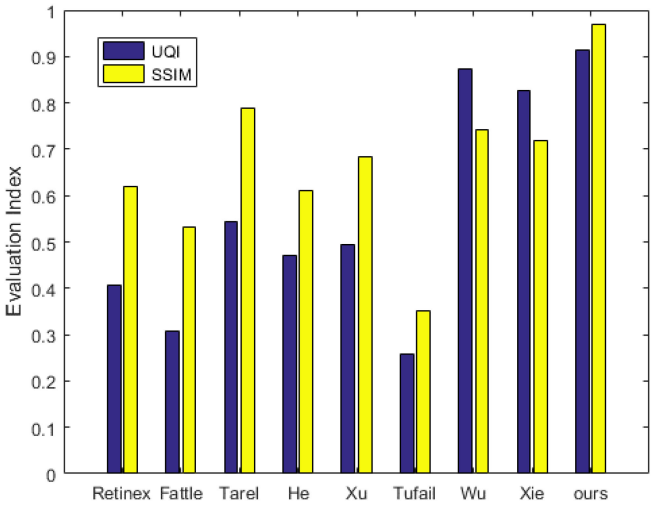

Fig. 26. Results bar chart of UQI and SSIM.

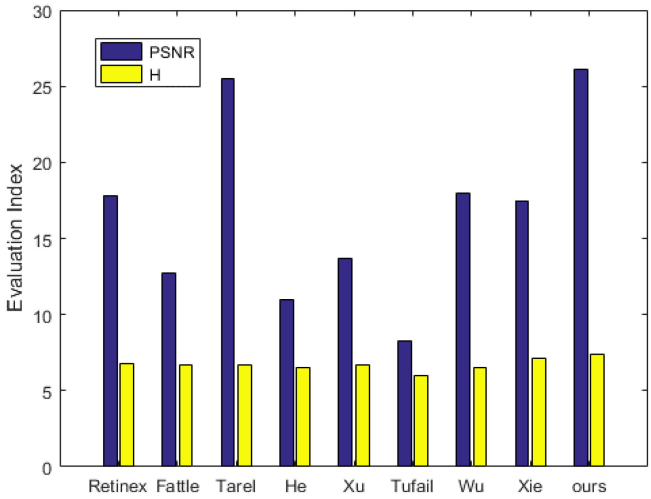

Fig. 27. Results bar chart of PSNR and *H*.

by Tufail's [66] appears blue. Wu's method [67] produces a noticeable distortion, with the color of the middle area of the image changing from gray to brown. The middle area of the restored image based on Xie's method [68] appears brown and the surrounding area appears light blue, resulting in different degrees of color distortion. On the contrary, image defogged by ADPF has the best performance with the least distortion and significantly improved contrast.

Table X shows the objective evaluation results of airport remote sensing image by using UQI, SSIM, PSNR, and information entropy *H*. Fig. 26 shows the bar chart of UQI and SSIM corresponding to Table X, and Fig. 27 shows the bar chart of PSNR and information entropy *H* corresponding to Table X. As shown above, our ADPF obtains the best performance for the four indicators.

Based on the five set of comparative experiments, the restored image of the proposed algorithm obtains more detail information, high contrast, and the least distortion. Abundant experiments demonstrate that the proposed method shows superior performance compared with other state-of-the-art methods.

V. CONCLUSION

Based on the DCP, In this article, we proposed a UAV sensing image defogging method named ADPF. First, we proposed an improved ASM to calculate the transmission and atmospheric light. Then, the grayscale image of the foggy image is adopted as the guidance image to refine the transmission. The adaptive compensation function was utilized to improve the low transmission of the sky or high light area so as to obtain accurate estimated transmission and image without distortion. Finally, through the quality evaluation, it was concluded that the proposed algorithm achieved the best performance in both image definition and quality. The fog-free image obtained clear detailed information and obvious structure, which was suitable for observation and analysis. Although our method achieved good performance, we still needed to continue further improvements and strive to increase the calculated speed so as to apply it to real-time defogging system.

REFERENCES

[1] A. Constantin and R. N. Dinculescu, "UAV development and impact in the power system," in *Proc. 8th Int. Conf. Modern Power Syst.*, 2019, pp. 1–5.
[2] Y. Wan *et al.*, "Tailings reservoir disaster and environmental monitoring using the UAV-ground hyperspectral joint observation and processing: A case of study in Xinjiang, the belt and road," in *Proc IEEE Int. Geosci. Remote Sens. Symp.*, 2019, pp. 9713–9716.
[3] D. J. Mulla, "Twenty five years of remote sensing in precision agriculture: Key advances and remaining knowledge gaps," *Biosyst. Eng.*, vol. 114, no. 4, pp. 358–371, 2013.
[4] C. Holness *et al.*, "Remote sensing archeological sites through unmanned aerial vehicle (UAV) imaging," in *Proc. IEEE Int. Geosci. Remote Sens. Symp.*, 2016, pp. 6695–6698.
[5] Y. Li *et al.*, Geometric correction algorithm of UAV remote sensing image for the emergency disaster," in *Proc. IEEE Int. Geosci. Remote Sens. Symp.*, 2016, pp. 6691–6694.

[6] B. Kellenberger, M. Volpi, and D. Tuia, "Fast animal detection in UAV images using convolutional neural networks," in *Proc. IEEE Int. Geosci. Remote Sens. Symp.*, 2017, pp. 866–869.

[7] T. Gao, Z. Liu, J. Cao, and S. Liang, "Local difference ternary sequences descriptor based on unsupervised min redundancy mutual information feature selection," *Multidimensional Syst. Signal Process.*, vol. 31, pp. 771–791, 2020.

[8] M. Ma, S. Mei, S. Wan, J. Hou, Z. Wang, and D. D. Feng, "Video summarization via block sparse dictionary selection," *Neurocomputing*, vol. 378, pp. 197–209, 2020.

[9] L. Xu *et al.*, "IDeRs: Iterative dehazing method for single remote sensing image," *Inf. Sci.*, vol. 489, pp. 50–62, 2019.

[10] W. Kim, "Image enhancement using patch-based principal energy analysis," *IEEE Access*, vol. 6, pp. 72620–72628, 2018.

[11] S. Mei, R. Jiang, X. Li, and Q. Du, "Spatial and spectral joint super-resolution using convolutional neural network," *IEEE Trans. Geosci. Remote Sens.*, vol. PP, no. 99, 2020, pp. 1–14, doi: 10.1109/tgrs.2020.2964288.

[12] G. Li, J. F Wu, and Z. Y. Lei, "Research progress of image haze grade evaluation and dehazing technology," *Laser J.*, vol. 35, no. 9, pp. 1–6, 2014.

[13] D. Wu and Q. Zhu, "The latest research progress of image dehazing," *Acta Autom. Sin.*, vol. 41, no. 2, pp. 221–239, 2015.

[14] A. K. Tripathi and S. Mukhopadhyay, "Removal of fog from images: A review," *IETE Tech. Rev.*, vol. 29, no. 2, pp. 148–156, 2012.

[15] L. Li *et al.*, "Color image enhancement using nonlinear sub-block overlapping local equilibrium algorithm under fog and haze weather conditions," *Trans. Beijing Inst. Technol.*, vol. 33, no. 5, pp. 516–522, 2013.

[16] S. C Huang, B. H Chen, and W. J. Wang, "Visibility restoration of single hazy images captured in real-world weather conditions," *IEEE Trans. Circuits Syst. Video Technol.*, vol. 24, no. 10, pp. 1814–1824, Oct. 2014.

[17] T. Fan *et al.*, "An improved single image defogging method based on Retinex," in *Proc. 2nd Int. Conf. Image, Vis. Comput.*, 2017, pp. 410–413.

[18] V. Magudeeswaran and J. F. Singh, "Contrast limited fuzzy adaptive histogram equalization for enhancement of brain images," *Int. J. Imag. Syst. Technol.*, vol. 27, no. 1, pp. 98–103, 2017.

[19] C. Busch and E. Debes, "Wavelet transform for analyzing fog visibility," *IEEE Intell. Syst. Their Appl.*, vol. 13, no. 6, pp. 66–71, Nov./Dec. 1998.

[20] Z. Ma and W. Jie, "Single-scale Retinex sea fog removal algorithm fused the edge information," *J. Comput.-Aided Des. Comput. Graph.*, vol. 27, no. 2, pp. 217–225, 2015.

[21] E. H. Land and J. McCann, "Lightness and Retinex theory," *J. Opt. Soc. Amer.*, vol. 61, no. 1, pp. 1–11, Jan. 1971.

[22] Z.-U. Rahman, D. J. Jobson, and G. A. Woodell, "Retinex processing for automatic image enhancement," *J. Electron. Imag.*, vol. 13, no. 1, pp. 100–110, Jan. 2004.

[23] D. J. Jobson, Z.-U. Rahman, and G. A. Woodell, "Properties and performance of a center/surround Retinex," *IEEE Trans. Image Process.*, vol. 6, no. 3, pp. 451–462, Mar. 1997.

[24] D. J. Jobson, Z. Rahman, and G. A. Woodell, "A multiscale Retinex for bridging the gap between color images and the human observation of scenes," *IEEE Trans Image Process.*, vol. 6, no. 7, pp. 965–976, Jul. 1997.

[25] M. Xue *et al.*, "Video image dehazing algorithm based on multi-scale Retinex with color restoration," in *Proc. Int. Conf. Smart Grid Elect. Automat.*, 2016, pp. 195–200.

[26] M. Elad, "Retinex by two bilateral filters," in *Proc. International Conference on Scale-Space Theories in Computer Vision*. Berlin, Heidelberg: Springer, 2005, pp. 217–229.

[27] Y. Liu *et al.*, "Criteria to evaluate the fidelity of image enhancement by MSRCR," *IET Image Process.*, vol. 12, no. 6, pp. 880–887, 2018.

[28] J. Shen *et al.*, "Exposure fusion using boosting Laplacian pyramid," *IEEE Trans. Cybern.*, vol. 44, no. 9, pp. 1579–1590, Sep. 2014.

[29] C. Y. Wong *et al.*, "Histogram equalization and optimal profile compression based approach for colour image enhancement," *J. Vis. Commun. Image Representation*, vol. 38, pp. 802–813, 2016.

[30] F. Yanjia and S. Feng, "Contrast adjustment based on image retrieval," *Laser Optoelectron. Prog.*, vol. 55, no. 5, 2018, Art. no. 051002.

[31] A. Pugazhenthi and L. S. Kumar, "Image contrast enhancement by automatic multi-histogram equalization for satellite images," in *Proc. 4th Int. Conf. Signal Process., Commun. Netw.*, 2017, 1–4.

[32] S. Yelmanov and Y. Romanyshyn, "Image contrast enhancement using a modified histogram equalization," in *Proc. IEEE 2nd Int. Conf Data Stream Mining Process.*, 2018, pp. 568–573.

[33] X. Ji *et al.*, "Real-time defogging processing of aerial images," in *Proc. 6th Int. Conf. Wireless Commun. Netw. Mobile Comput.*, 2010, pp. 1–4.

[34] S. Huang *et al.*, "Haze removal algorithm for optical remote sensing image based on multi-scale model and histogram characteristic," *IEEE Access*, vol. 7, pp. 104179–104196, 2019.

[35] S. Dippel, M. Stahl, R. Wiemker, and T. Blaffert, "Multiscale contrast enhancement for radiographies: Laplacian pyramid versus fast wavelet transform," *IEEE Trans. Med. Imag.*, vol. 21, no. 4, pp. 343–353, Apr. 2002.

[36] J. Jia and H. Yue, "A wavelet-based approach to improve foggy image clarity," *IFAC Proc. Vol.*, vol. 47, no. 3, pp. 930–935, 2014.

[37] Y. Yang *et al.*, "A novel single image dehazing method," in *Proc. Int. Conf. Comput. Problem-Solving*, 2013, pp. 275–278.

[38] D. Qi'an, X. Xiaoguang, and W. Zhen, "The image optimization algorithm based on channel prior and wavelet transform," *J. Sichuan Univ. Sci. Eng.*, vol. 31, no. 5, pp. 43–48, 2018.

[39] M. Ju, Z. Gu, and D. Zhang, "Single image haze removal based on the improved atmospheric scattering model," *Neurocomputing*, vol. 260, pp. 180–191, 2017.

[40] E. J. McCartney, *Optics of the Atmosphere: Scattering by Molecules and Particles*. New York, NY, USA: Wiley, 1976.

[41] Y. Jiang *et al.*, "Fog density estimation and image defogging based on surrogate modeling for optical depth," *IEEE Trans. Image Process.*, vol. 26, no. 7, pp. 3397–3409, Jul. 2017.

[42] E. Namer and Y. Y Schechner, "Advanced visibility improvement based on polarization filtered images," *Proc. SPIE*, vol. 5888, 2005, Art. no. 588805.

[43] S. G Narasimhan and S. K Nayar, "Interactive (de) weathering of an image using physical models," in *Proc. IEEE Workshop Color Photometric Methods Comput. Vis.*, 2003, vol. 6, no. 6.4, p. 1.

[44] S. K. Nayar and S. G. Narasimhan, "Vision in bad weather," in *Proc. 7th IEEE Int. Conf. Comput. Vis.*, 1999, vol. 2, pp. 820–827.

[45] S. G. Narasimhan and S. K. Nayar, "Vision and the atmosphere," *Int. J. Comput. Vis.*, vol. 48, no. 3, pp. 233–254, 2002.

[46] W. Wang *et al.*, "A fast single-image dehazing method based on a physical model and gray projection," *IEEE Access*, vol. 6, pp. 5641–5653, 2018.

[47] Y. Jiang *et al.*, "Fog density estimation and image defogging based on surrogate modeling for optical depth," *IEEE Trans. Image Process.*, vol. 26, no. 7, pp. 3397–3409, Jul. 2017.

[48] E. Namer and Y. Y. Schechner, "Advanced visibility improvement based on polarization filtered images," *Proc SPIE.*, vol. 5888, 2005, Art. no. 588805.

[49] Y. Y Schechner, S. G. Narasimhan, and S. K. Nayar, "Polarization-based vision through haze," *Appl. Opt.*, vol. 42, no. 3, pp. 511–525, 2003.

[50] Y. Y. Schechner, S. G. Narasimhan, and S. K. Nayar, "Instant dehazing of images using polarization," in *Proc. IEEE Comput. Soc. Conf. Comput. Vis. Pattern Recognit.*, 2001, pp. 325–332.

[51] S. Shwartz, E. Namer, and Y. Y Schechner, "Blind haze separation," in *Proc. IEEE Comput. Soc. Conf. Comput. Vis. Pattern Recognit.*, 2006, vol. 2, pp. 1984–1991.

[52] X. Dong *et al.*, "Fast efficient algorithm for enhancement of low lighting video," in *Proc. IEEE Int. Conf. Multimedia Expo.*, 2011, pp. 1–6.

[53] K. Nishino, L. Kratz, and S. Lombardi, "Bayesian defogging," *Int. J. Comput. Vis.*, vol. 98, no. 3, pp. 263–278, 2012.

[54] R. Fattal, "Single image dehazing," *ACM Trans. Graph.*, vol. vol. 27, no. 3, pp. 72:1–72:10, Aug. 2008.

[55] J. P. Tarel and N. Hautiere, "Fast visibility restoration from a single color or gray level image," in *Proc. IEEE 12th Int. Conf. Comput. Vis.*, 2009, pp. 2201–2208.

[56] R. T. Tan, "Visibility in bad weather from a single image," in *Proc. IEEE Conf. Comput. Vis. Pattern Recognit.*, 2008, pp. 1–8.

[57] K. He, J. Sun, and X. Tang, "Single image haze removal using dark channel prior," *IEEE Trans. Pattern Anal. Mach. Intell.*, vol. 33, no. 12, pp. 2341–2353, Dec. 2010.

[58] C. Huang *et al.*, "Improved algorithm for image haze removal based on dark channel priority," *Comput. Elect. Eng.*, vol. 70, pp. 659–673, 2018.

[59] Z. Chen *et al.*, "Research of polarized image defogging technique based on dark channel priori and guided filtering," *Procedia Comput. Sci.*, vol. 131, pp. 289–294, 2018.

[60] T. Sheng and Q. Chen, "Dark channel prior-based altitude extraction method for a single mountain remote sensing image," *IEEE Geosci. Remote Sens. Lett.*, vol. 14, no. 1, pp. 132–136, Jan. 2016.

[61] M. Xiao *et al.*, "Intelligent defogging method based on clustering and dark channel prior," in *Proc. IEEE 3rd Int. Conf. Image, Vis. Comput.*, 2018, pp. 149–156.

[62] S. Lee *et al.*, "A review on dark channel prior based image dehazing algorithms," *EURASIP J. Image Video Process.*, vol. 2016, no. 1, p. 4, 2016.

[63] L. Shi *et al.*, "Image haze removal using dark channel prior and minimizing energy function," in *Proc. IEEE 2nd Inf. Technol., Netw., Electron. Automat. Control Conf.*, 2017, pp. 256–259.
[64] M. Hu *et al.*, "Single image dehazing based on dark channel prior and energy minimization," *IEEE Signal Process. Lett.*, vol. 25, no. 2, pp. 174–178, Feb. 2018.
[65] Y. Xu *et al.*, "Single image haze removal using light and dark channel prior," in *Proc. IEEE/CIC Int. Conf. Commun. China*, 2016, pp. 1–6.
[66] Z. Tufail *et al.*, "Improved dark channel prior for image defogging using RGB and YCbCr color space," *IEEE Access*, vol. 6, pp. 32576–32587, 2018.
[67] K. Wu *et al.*, "Multi-scale guided filter and its application in image," *Opt. Precis. Eng.*, vol. 25, no. 8, pp. 2182–2194, 2017.
[68] L. Xie *et al.*, "A novel haze removal algorithm for atmospheric degraded image with dark channel prior," *Control Eng. China*, vol. 27, no. 02, pp. 207–211, 2020.
[69] Q. Yuan, H. Shen, and H. Li, "Single remote sensing image haze removal based on spatial and spectral self-adaptive model," in *Proc. Int. Conf. Image Graph*, 2015, pp. 382–392.
[70] W. Fengping and W. Weixing, "Road extraction using modified dark channel prior and neighborhood FCM in foggy aerial images," *Multimedia Tools Appl.*, vol. 78, no. 1, pp. 947–964, 2019.
[71] J. Zhang *et al.*, "Image dehazing based on dark channel prior and brightness enhancement for agricultural remote sensing images from consumer-grade cameras," *Comput. Electron. Agric.*, vol. 151, pp. 196–206, 2018.
[72] J. Long *et al.*, "Single remote sensing image dehazing," *IEEE Geosci. Remote Sens. Lett.*, vol. 11, no. 1, pp. 59–63, Jan. 2013.
[73] K. He, J. Sun, and X. Tang, "Guided image filtering," *European Conference on Computer Vision*. Berlin, Germany: Springer, 2010, pp. 1–14.
[74] K. Ma, W. Liu, and Z. Wang, "Perceptual evaluation of single image dehazing algorithms," in *Proc. IEEE Int. Conf. Image Process.*, 2015, pp. 3600–3604.
[75] ITU-R BT.500-12, "Recommendation: Methodology for the subjective assessment of the quality of television pictures," Nov. 1993.
[76] Z. Wang, A. C. Bovik, H. R. Sheikh, and E. P. Simoncelli, "Image quality assessment: From error visibility to structural similarity," *IEEE Trans. Image Process.*, vol. 13, no. 4, pp. 600–612, Apr. 2004.
[77] M. Carnec, P. Le Callet, and D. Barba, "Objective quality assessment of color images based on a generic perceptual reduced reference," *Signal Process., Image Commun.*, vol. 23, no. 4, pp. 239–256, Apr. 2008.
[78] H. R. Sheikh, A. C. Bovik, and L. Cormack, "No-reference quality assessment using natural scene statistics: JPEG2000," *IEEE Trans. Image Process.*, vol. 14, no. 1, pp. 1918–1927, Nov. 2005.
[79] Z. Wang and A. C. Bovik, "A universal image quality index," *IEEE Signal Process. Lett.*, vol. 9, no. 3, pp. 81–84, 2002.
[80] T. Hao-nan and L. Su-mei, "Objective evaluation method for image quality based on edge structure similarity," *Acta Photon. Sin.*, vol. 42, no. 01, pp. 110–114, 2013.
[81] W. Yuanji *et al.*, "Image quality evaluation based on image weighted separating block peak signal to noise ratio," in *Proc. Int. Conf. Neural Netw. Signal Process.*, 2003, vol. 2, pp. 994–997.
[82] Z. Su-Ru, "An image information entropy-based algorithm of no-reference image quality assessment," master dissertation, Beijing Jiaotong University, Beijing, China, 2015.
[83] M. Ju, D. Zhang, and X. Wang," Single image dehazing via an improved atmospheric scattering model," *Vis. Comput.*, vol. 33, no. 12, pp. 1613–1625, 2017.
[84] Z. Zhenghao *et al.*, "An improved aerial remote sensing image defogging method based on dark channel prior information," *J. Geomatics Sci. Technol.*, vol. 35, no. 02, pp. 182–186, 2018.

Tao Gao received the B.Sc., M.Sc., and Ph.D. degrees in information and communication engineering from the School of Electronics and Information, Northwestern Polytechnical University, Xi'an, China, in 2002, 2016, and 2010, respectively.

He is currently with the School of Information Engineering, Chang'an University, Xi'an, China. His current research interests include image processing and computer vision.

Kun Li received the B.Sc. degree in information and communication engineering from the School of Electronic Information and Electrical Engineering, Anyang Institute of Technology, Anyang, China, in 2017.

He is currently with the School of Information Engineering, Chang'an University, Xi'an, China. His current research interests include image processing and Java software development.

Ting Chen received the Ph.D. degree in information and communication engineering from Xi'dian University, Xi'an, China, in 2011.

She is currently a Lecturer with the School of Information Engineering, Chang'an University, Xi'an, China. Her current research interests include signal processing and wireless networks.

Mengni Liu received the B.Sc. degree in information and communication engineering from the School of Communication and Information Engineering, North China University of Science and Technology, Qinhuangdao, China, in 2019.

She is currently with the School of Information Engineering, Chang'an University, Xi'an, China. Her current research interests include image processing and Java software development.

Shaohui Mei received the B.Sc. degree in electronics and information engineering and the Ph.D. degree in signal and information processing from Northwestern Polytechnical University, Xi'an, China, in 2005 and 2011, respectively.

He is currently an Associate Professor with the School of Electronics and Information, Northwestern Polytechnical University, Xi'an, China. From October 2007 to October 2008, he was a Visiting Student with the University of Sydney. His current research interests include hyperspectral remote sensing image processing, deep learning, and video processing and pattern recognition.

Ke Xing received the B.Sc. degree in information and communication engineering from the School of Communication Engineering, Shaanxi University of Technology, Hanzhong, China, in 2019.

She is currently with the School of Information Engineering, Chang'an University, Xi'an, China. Her current research interests include image processing and Java software development.

Yong Hui Li photograph and biography not available at the time of publication.